Journal of Scientific & Industrial Research
Vol. 85, May 2026, pp. 395-410
DOI: 10.56042/jsir.v85i5.20419

# A Robust Control Framework Using DISMC-KY Converter and Feedforward Fast Decoupled Current Controlled Inverter for Grid Integrated Solar EV Charging

Anjumol C S* & Preethi Thekkath

Dept. of Electrical and Electronics Engineering, Toc H Institute of Science and Technology, APJ Abdul Kalam Technological University, Trivandrum 695 016, Kerala, India

*Received 06 June 2025; revised 30 December 2025; accepted 29 July 2026*

The increasing adoption of Electric Vehicles (EV s) and renewable energy integration has highlighted the need for efficient Photovoltaic (PV)-based EV charging systems with surplus power export capability. However, on the DC side Partial Shading Conditions (PSC) affects Maximum Power Point Tracking (MPPT) performance, while traditional converters introduce high ripple and discontinuous currents, limiting PV energy utilization. On the AC side, conventional inverter control suffers from cross-coupling effects, resulting in poor dynamic response, high THD and reduced grid-code compliance, leading to inefficient EV charging performance. To overcome these limitations, this paper proposes a grid integrated PV-EV charging system employing an Incremental Conductance (InC) MPPT based Double Integral Sliding Mode Controlled (DISMC) KY converter for DC–DC conversion and a Feed-Forward Fast Decoupled Current Control (FF-FDCC) strategy for inverter regulation. The DISMC-controlled KY converter suppresses chattering, achieves rapid MPPT convergence with negligible steady-state error and thereby enhances power-conversion efficiency, resulting in higher charging current and reduced EV charging time. On the AC side, the FF-FDCC strategy eliminates d–q cross coupling effect with minimal sensor dependency. Spectral analysis confirms significant suppression of switching harmonics and conducted EMI, with grid current THD reduction within IEEE limit. The proposed approach enables dynamic reactive power compensation without controller re-tuning. A state-space-based power management scheme enables seamless transition between PV to EV charging mode and grid export mode, maximizing solar energy utilization. Simulation studies and hardware validation confirm accurate MPPT tracking under PSC and robust grid side stability is verified through Lyapunov and Bode plot analyses.

**Keywords:** DC-DC converter, Electromagnetic compatibility, Nonlinear control, Partial shading conditions, Power quality improvement

## Introduction

The rapid adoption of EVs has accelerated the need for renewable energy-based charging infrastructures that ensure efficient, reliable and sustainable energy transfer. Among these PV charging systems have emerged as a promising solution supporting clean energy integration, while reducing dependence on fossil fuels and enhancing grid stability through bidirectional power flow. However, conventional grid-connected PV–EV charging systems face several challenges, including inefficient MPPT tracking under PSC, high THD, voltage instability, slow dynamic response, and inefficient power conversion. These limitations reduce PV energy extraction, unstable power injection into the grid, increase in EV charging time, ultimately degrading overall system efficiency and power quality.

Although the InC MPPT algorithm is widely adopted due to its simple structure and ease of practical implementation, its conventional formulation exhibits slow tracking dynamics and persistent oscillations under rapidly varying irradiance conditions, which has motivated recent efforts to enhance the InC framework rather than replace it.[1] While metaheuristic MPPT techniques can achieve high tracking accuracy, their computational intensity and algorithmic complexity restrict their suitability for real-time embedded EV charging applications. Consequently, several studies have focused on augmenting InC with advanced control concepts, such as hybrid InC–integral backstepping control, InC combined with Sliding Mode Control (SMC), and optimization assisted tuning such as Harris Hawks Optimization, to enhance robustness and convergence under PSC.[2–4] Similarly, fuzzy-logic-based InC approaches improve tracking efficiency but impose additional tuning and computational burdens.[5] This necessitates the development of an advanced control for InC-based MPPT strategy that combines robust nonlinear control with implementation simplicity.

*Author for Correspondence
E-mail: anjumolcs@tistcochin.edu.in

Beyond control algorithms, the choice of DC–DC converter topology significantly influences PV–EV charging performance. Conventional converters such as buck, boost, buck–boost, SEPIC, and Ćuk are widely used but often suffer from high current and voltage ripple, limited voltage gain, poor transient response, and reduced efficiency under PSC and dynamic load conditions.[6,7] These issues affect MPPT accuracy and EV battery performance. Although non-isolated converters offer compact designs, they face challenges under wide voltage variations.[8] High density converters require complex thermal management, while dual input converters and IoT enabled flyback designs introduce additional control complexity and efficiency degradation at high load levels.[9,10] Interleaved and cascaded structures reduce ripple but increase system size, cost and design complexity, which is undesirable for compact EV charging applications.[11,12] In this context, the KY converter has emerged as a promising alternative owing to its ripple-free input and output currents, continuous conduction mode (CCM) operation, low voltage ripple, and simple structural design ,however its potential in PV–EV charging applications remains largely unexplored.[13,14]

Advanced nonlinear control techniques have been extensively investigated to control DC-DC converter to enhance MPPT performance. SMC is well known for its robustness to uncertainties and disturbances, but its conventional form suffers from chattering, leading to increased EMI and reduced component life-time.[15] Advanced variants such as higher order SMC, super twisting SMC and DISMC have been proposed to mitigate these issues.[16–21] Among these, DISMC offers improved dynamic response with reduced steady-state error and suppressed chattering while maintaining implementation simplicity. However, existing DISMC based MPPT implementations are almost exclusively limited to boost-type converters and their application to KY converters remains unexplored. Although adaptive and hybrid SMC techniques such as Adaptive Sliding Mode Control (ASMC), Circle Search Algorithm–Based Super-Twisting (CSA-ST )SMC and Super Twisting Higher-Order Sliding Mode Control (ST-HOSMC) have improved dynamic robustness tracking accuracy, and have mitigated chattering, but they often require complex gain tuning, heavy computation and lack hardware validation.[22–24] Similarly, AI assisted MPPT controllers provide predictive adaptability but depend on large training datasets and high processing resources.[25,26] Also, hybrid model based and data driven MPPT strategies, while achieving enhanced tracking accuracy and adaptability, often incur greater computational overhead and integration complexity, limiting their feasibility for real time, resource constrained PV- EV charging applications.[27]

On the grid side, inverter control is crucial for maintaining power quality, grid-code compliance, and stable interaction between PV–EV systems and the utility grid. Existing feed forward decoupling and direct power control strategies improve transient response but typically operate at the power-control level without explicitly compensating d–q axis coupling in the current loop, resulting in residual interactions under dynamic conditions.[28,29] Hysteresis-based controllers exhibit variable switching frequency and increased EMI, complicating filter design, while sensor-reduced and active damping methods may compromise dynamic performance or introduce estimation sensitivity and additional tuning requirements.[30,31] Although research on Vehicle-to-Grid (V2G) area has advanced toward bidirectional power exchange and ancillary services, practical deployment remains limited by inverter performance degradation during grid impedance variations and frequent mode transitions, leading to reactive power oscillations and harmonic distortion.[32,33]

Motivated by these gaps, this paper proposes an integrated PV–EV charging framework combining a DISMC-controlled KY converter for DC-side MPPT optimization and a feedforward fast decoupled current control strategy for AC-side inverter regulation. The system operates in two modes: PV-to-EV charging (P2V) and PV-to-grid power export (P2G).

The main contributions are summarized as follows:

1. A DISMC-based MPPT formulation for the KY converter is introduced for PV–EV charging, achieving ripple-free operation, reduced chattering, negligible steady-state error, and fast global MPP tracking under PSC, thereby improving power utilization and reducing EV charging time.
2. A hardware-feasible enhancement of the InC MPPT algorithm is developed by integrating DISMC, avoiding the computational complexity of AI- and optimization-based MPPT approaches.
3. A FF-FDCC inverter control strategy is proposed to eliminate $d$–$q$ axis cross-coupling at the current-control level, enabling fixed switching frequency operation, dynamic reactive power compensation without controller re-tuning,

and mitigation of switching-harmonic-induced EMI.

4. A unified DC–AC control and state-space-based power management framework is developed to ensure seamless transition between P2V and P2G modes under dynamic irradiance, load, and grid conditions.
5. A three-level validation framework is implemented, including 40 W experimental validation, 400 W system-level verification, and 25 kW large-scale simulation, evaluating charging performance, grid power quality, stability, and standards compliance.

## PV based EV Charging System Configuration

The overall architecture of the proposed PV-based EV charging system with grid integration is depicted in Fig. 1. The PV array generates voltage $V_{pv}$ and current $I_{pv}$, while the InC algorithm tracks the MPP by adjusting the duty cycle using the condition $dI_{pv}/dV_{pv} = -I_{pv}/V_{pv}$.[34] The resulting voltage error is processed by the DISMC module to regulate the KY converter through PWM, ensuring accurate MPPT. Based on mode selection, power is then distributed by power management module either to the DC-DC charger for EV charging or to inverter for grid injection. A bidirectional buck–boost DC–DC charger maintains the DClink voltage at 500V

## KY Converter Modelling

The proposed DISMC controlled KY converter illustrated in Fig. 2, comprises two MOSFET switches ($S_1$, $S_2$), a diode (D), an energy transfer capacitor ($C_b$), an energy transfer inductor (L), and an output capacitor ($C_o$). This configuration enables continuous conduction operation with reduced voltage and current ripple.

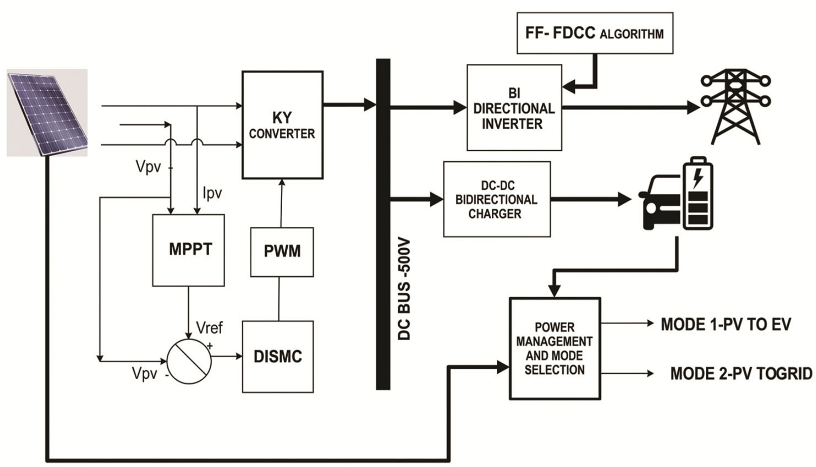


Fig. 1 — Schematic of proposed grid integrated PV charging of EV

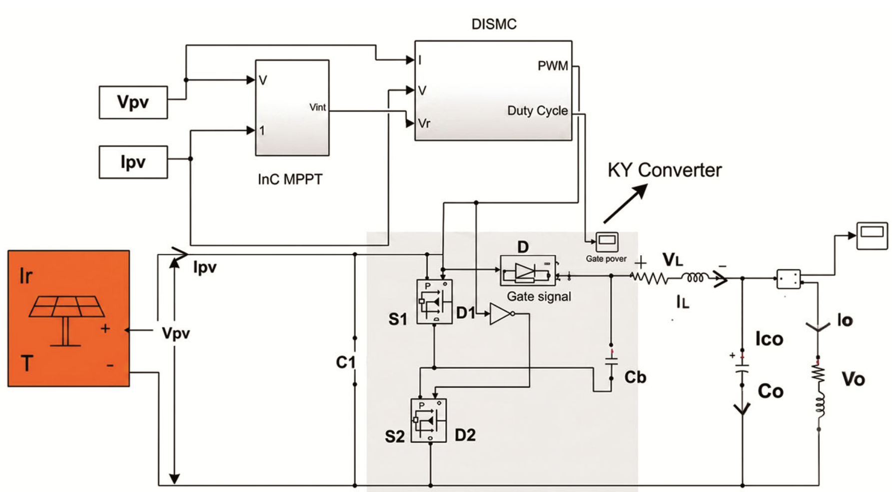


Fig. 2 — Proposed MATLAB model of DISMC controlled KY converter

In Mode 1 operation of the KY converter, switch $S_1$ is ON, $S_2$ is OFF and diode D is reverse-biased. During this interval, the inductor L operates in its energy storage phase, resulting in a rising inductor current $I_L$. This energy helps charge the capacitor, ensuring a smooth output voltage ($V_o$). As initial voltage of $V_{cb}= V_{pv}$.

$$V_{L1} = 2V_{pv} - V_o \quad \ldots (1)$$

where, $V_{L1}$ is the inductor voltage during ON period of $S_1$.

Also $$\dot{I}_{L1} = \frac{2}{L}V_{pv} - \frac{1}{L}V_o \quad \ldots (2)$$

$$\dot{V_{pv}} = \frac{1}{C_b}I_{L1} \quad \ldots (3)$$

where, $I_L = I_{pv} = I_{cb}$, and $\dot{I}_{L1}$ is the inductor current dynamics and $\dot{V_{pv}}$ is the PV voltage dynamics in Mode 1

During Mode 2 operation, when switch $S_2$ is turned ON and switch $S_1$ is turned OFF, the inductor L enters a demagnetization phase. Mathematically,

$$V_{L2} = V_{pv} - V_o \quad \ldots (4)$$

where, $V_{L2}$ is the voltage across the inductor L during Mode 2. The inductor current dynamics and PV voltage dynamics in this mode are given by:

$$\dot{I}_{L2} = \frac{1}{L}V_{pv} - \frac{1}{L}V_o \quad \ldots (5)$$

$$\dot{V}_{pv} = \frac{1}{C_b r_{pv}}V_{pv} - \frac{1}{C_b}I_{L2} \quad \ldots (6)$$

where, $r_{pv} = 1/g_{pv}$ be the incremental resistance of the PV panel and $g_{pv} = \frac{dI_{pv}}{dV_{pv}}$ be the incremental conductanc. Applying volt-sec balance, the average voltage across the inductor

$$V_L = \delta V_{L1} + (1-\delta)V_{L2} = 0 \quad \ldots (7)$$

$$\frac{V_0}{V_{pv}} = 1 + \delta \quad \ldots (8)$$

where, δ (delta) is the duty ratio KY converter

For analysis in this particular model, state variables of the KY converter,

$$X = \begin{bmatrix} x_1 \\ x_2 \end{bmatrix} = \begin{bmatrix} I_L \\ V_{pv} \end{bmatrix} \quad \ldots (9)$$

where, $x_1$ and $x_2$. are chosen as inductor current ($I_L$) and input voltage ($V_{pv}$) respectively.

The state space equations can be written as

$$\text{Mode 1: } \dot{x}_{11} = \frac{2}{L}x_2 - \frac{1}{L}V_0,\ \dot{x}_{21} = \frac{1}{C_b}x_1 \quad \ldots (10)$$

$$\text{Mode 2: } \dot{x}_{12} = \frac{1}{L_1}x_2 - \frac{1}{L}V_0,\ \dot{x}_{22} = \frac{1}{C_b r_{pv}}x_2 - \frac{1}{C_b}x_1 \quad \ldots (11)$$

The state equation for the complete time period can be written as

$$\dot{x}_1 = \frac{(1+\delta)}{L}x_2 - \frac{1}{L}V_0,\ \dot{x}_2 = \frac{(2\delta-1)\,x_1 + (1-\delta)\frac{1}{r_{pv}}x_2}{C_b} \quad \ldots (12)$$

where, duty ratio of the control signal u is defined as $\delta$ for controlling the switches in KY converters,

Hence state space dynamics of the KY converter can be written as

$$\dot{X} = f(X, t) + g(X,t)u \quad \ldots (13)$$

where, $f(X) = \begin{bmatrix} \frac{x_2 - V_0}{L} \\ \frac{\frac{1}{r_{pv}}x_2 - x_1}{C_b} \end{bmatrix}$ and $g(X) = \begin{bmatrix} \frac{x_2}{L} \\ 0 \end{bmatrix}$

where, $0 \le u \le 1$, for a DC/DC converter.

#### Proposed Sliding Surface Design for DISMC Control

Conventional KY converter control may produce increased output voltage ripple under dynamic conditions, affecting MPPT accuracy and system performance. To address this, the proposed DISMC extends classical SMC by employing a second-order sliding surface based on PV voltage tracking error and its integral to improve steady-state accuracy and suppress chattering.[35]

$$S = e = V_{pv} - V_{MPP} \quad \ldots (14)$$

where, S is the sliding surface and e is the tracking error

The control law (u) combines equivalent and discontinuous components to ensure stable sliding motion. Hence,

$$u = U_{eq} + U_n \quad \ldots (15)$$

where, $U_{eq}$= equivalent control and $U_n$ = non linear switching control.

At maximum output power, during the operation of PV array, proposed sliding surface (S) to be:

$$S = a_1e_1 + a_2e_2 + a_3e_3 + a_4e_4 \quad \ldots (16)$$

where, the terms $a_1$, $a_2$, $a_3$ and $a_4$ denote the sliding coefficients and $e_1$, $e_2$, $e_3$ and $e_4$ are various error signals and are defined as follows.

$$e_1 = I_{ref} - I_L \quad \ldots (17)$$

$$e_2 = V_{ref} - \beta V_{pv} \quad \ldots (18)$$

$$e_3 = \int (V_{ref} - \beta V_{pv})\, dt \quad \ldots (19)$$

$$e_4 = \iint (V_{ref} - \beta V_{pv})\, dt^2 \quad \ldots (20)$$

$$I_{ref} = \alpha(V_{ref} - \beta V_{pv}) \quad \ldots (21)$$

The sliding surface uses current and voltage errors to regulate inductor current and drive PV voltage to MPP. Integral terms reduce chattering and improve accuracy, ensuring coordinated MPPT and converter current control. The gain parameter α in the reference current generation equation is closely related to the inductance (L) and capacitance (C) of the KY converter, as it governs the dynamic response of the control system. Value of α typically ($0 < \alpha < 1$), selected based on the system's LC time constant to ensure fast yet stable tracking of the maximum power point. The parameter β plays a crucial role in scaling the PV voltage to accurately track the reference current, ensuring precise MPPT operation. β can be fine-tuned (between 0.9 and 1.1) during simulation to improve tracking accuracy or reduce sensitivity to measurement noise.

The switching control law: $U_n = \begin{Bmatrix} 0\ ;\ S \geq 0 \\ 1\ ;\ S < 0 \end{Bmatrix} \quad \ldots (22)$

In order for the suggested strategy to work, $U_{eq}$ is obtained from the invariance condition

$$(S(x) = 0\ ;\ \dot{S}(x) = 0) \Rightarrow (u \cong Ueq) \quad \ldots (23)$$

The equivalent signal ($U_{eq}$) can be calculated by solving above equation as $dS(x)=0$

$$dS = \left(\frac{\partial R}{\partial I_{pv}} - \frac{\partial r}{\partial I_{pv}}\right)\frac{dIpv}{\partial t} \quad \ldots (24)$$

Eq. (23) can be rewritten as: $dS = A\frac{dI_L}{dt} = A\left(\frac{(1+\delta)}{L}V_{pv} - \frac{1}{L}V_0\right) \quad \ldots (25)$

where, A is an auxiliary coefficient defined as, $A = \left(\frac{\partial R}{\partial I_{pv}} - \frac{\partial r}{\partial I_{pv}}\right)$, Considering Eqs (22) and (24), the equivalent control input for KY Converter is obtained as

$$U_{eq} = \frac{V_o}{V_{pv}} - 1 = \text{Duty cycle} = \delta \quad \ldots (26)$$

To verify the stability, a nonlinear Lyapunov candidate function is selected as $V(x) = \frac{1}{2}S^2(x)$, where, $S(x)$denotes the sliding surface.[36] According to Lyapunov's stability theorem, system stability is guaranteed if the time derivative of the Lyapunov function satisfies $\dot{V}(x) = S(x)\dot{S}(x) < 0$, ensuring that $\dot{V}(x)$is negative definite. Accordingly, a nonlinear switching control law ($U\ \ n$)is designed to compensate for external disturbances and enforce convergence of the system trajectories toward the sliding manifold.

$$U_n = K[\,S(x)]^{\propto}\,\text{sat}\frac{S(x)}{\propto} \quad \ldots (27)$$

where, $\text{sat}\frac{S(x)}{\propto} = \begin{Bmatrix} 1\ ;\ \left|\text{sat}\frac{S(x)}{\propto}\right| \leq 1 \\ \text{sgn}\frac{S(x)}{\propto}\ ;\ \left|\text{sat}\frac{S(x)}{\propto}\right| > 0 \end{Bmatrix} \quad \ldots (28)$

For a given state, the approaching speed to the sliding surface increases when it is far from the sliding surface and decreases when it is close to the sliding surface due to the exponential term $\frac{S(x)}{\propto}$. The chattering magnitude is reduced by including input signal ($U_n$) in a barrier of thickness α. where, $0 < \alpha < 1$. The saturation function sat($\frac{S(x)}{\propto}$) is employed for smooth transition of control action near the sliding surface. Hence the control law for DISMC can be obtained as

$$u = U_{eq} + U_n = \delta + K[\,S(x)]^{\propto}\,\text{sat}\frac{S(x)}{\propto} \quad \ldots (29)$$

where, $u = \begin{Bmatrix} \delta + K; S > 0 \\ 0;\ S = 0 \\ \delta - K; S < 0 \end{Bmatrix} \quad \ldots (30)$

The duty cycle thus obtained from the DISMC is used for generating gate pulse for switching KY Converter.

## Feed-Forward Fast Decoupled Current Control (FF-FDCC) of Inverter in P2G mode

### System Structure and Power Coupling Analysis

The conventional *d–q* current control scheme for the grid-connected inverter is illustrated in Fig. 3.

Assuming a balanced three phase grid voltages neglecting zero sequence components, the three phase inverter dynamics are transformed from the abc reference frame to the synchronous d-q reference frame using Park's transformation. The grid

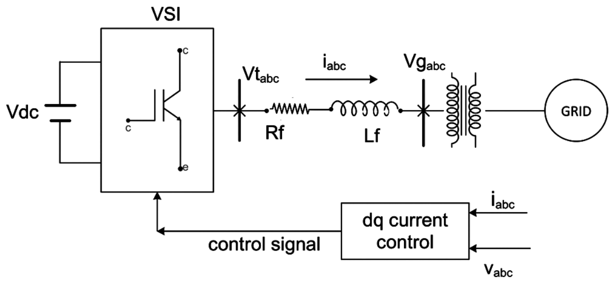


Fig. 3 — Structure of grid connected inverter

connected inverter model in the d-q frame can be expressed as:

$$V_{td}(s) = R_f I_d(s) + L_f s I_d(s) - \omega L_f I_q(s) + V_{gd} \quad \dots (31)$$

$$V_{tq}(s) = R_f I_q(s) + L_f s I_q(s) + \omega L_f I_d(s) + V_{gq} \quad \dots (32)$$

where, $V_{td}$ and $V_{tq}$ represent the d-q axis converter control voltages, $R_f$ and $L_f$ denote the filter resistance and inductance, respectively. The d-q axis currents are represented by Id and Iq, whereas Vgd and Vgq correspond to the d-q axis grid voltages. The rotation of the synchronous reference frame at angular frequency, ω ,introduces dq-axis cross coupling terms $\omega L_f I_q$ and $-\omega L_f I_d$, as shown in Eqs. (31,32), which adversely affect current tracking accuracy. To decouple these equations, a feedforward compensation term is introduced. The modified control input voltages including feedforward terms are

$$V_{tdref}(s) = V_{td}(s) + \omega L_f I_q(s) \quad \dots (33)$$

$$V_{tqref}(s) = V_{tq}(s) - \omega L_f I_d(s) \quad \dots (34)$$

Substituting in Eqs (31) and (32) gives the decoupled dynamics:

$$V_{tdref}(s) = R_f I_d(s) + L_f s I_d(s) + V_{gd} \quad \dots (35)$$

$$V_{tqref}(s) = R_f I_q(s) + L_f s I_q(s) + V_{gq} \quad \dots (36)$$

Now, the current responses become $I_d(s) = \frac{V_{tdref}(s) - V_{gd}}{R_f + L_f s}$ ... (37)

$$I_q(s) = \frac{V_{tqref}(s) - V_{gq}}{R_f + L_f s} \quad \dots (38)$$

To regulate the currents, a PI controller is introduced with transfer function $G_c(s) = K_p + \frac{K_i}{s}$, where, $K_p$ is proportional gain and $K_i$ is integral gain. The closed loop transfer function with the PI controller is:

$$V_{tdref}(s) = G_c(s)[I_{dref} - I_d](s) + V_{gd} \quad \dots (39)$$

$$V_{tqref}(s) = G_c(s)\left[I_{qref} - I_q\right](s) + V_{gq} \quad \dots (40)$$

where, $I_{dref}$ and $I_{qref}$ are the reference currents.

**Reference Current Generation Strategy in P2V and P2G Mode**

The active and reactive power for a balanced three phase system can be written in the synchronous d-q frame as follows

$$P = \frac{3}{2}(V_{gd} I_d + V_{gq} I_q) \text{ and } Q = \frac{3}{2}(V_{gq} I_d - V_{gd} I_q) \quad \dots (41)$$

Aligning the d-axis with the grid voltage vector yields $V_{gq} = 0$, resulting in $P = \frac{3}{2} V_{gd} i_d$ and $Q = -\frac{3}{2} V_{gd} i_q$.

In P2V Mode, the active power reference ($P_{ref}$) is determined based on the available PV surplus power

$$P_{ref} = P_{pv} - P_{loss} - P_{EV}. \quad \dots (42)$$

where, $P_{loss}$denotes system losses and $P_{EV}$is the EV charging power. Since all PV power is used for EV charging, $P_{ref} = 0$, resulting in $I_{dref} = 0$ and there is no grid power injection. In P2G mode ($P_{EV} = 0$), surplus PV power is exported to the grid. For unity power factor operation:

$$Q_{ref} = 0 \Rightarrow i_{q,ref} = i_{q,ref}^{UPF} = 0 \text{ and } i_{d,ref} = \frac{2}{3}\frac{P_{ref}}{V_{gd}} \quad \dots (43)$$

However, when grid voltage regulation is required, the reactive current reference ($i_{q,RC}$) is derived from PCC voltage error, $e_v = V_{ref} - V_{meas}$ ... (44)

where, $V_{ref}$ denotes the reference PCC voltage, and $V_{meas}$ represents the measured PCC voltage.

$$i_{q,RC} = \begin{cases} K_{p,v} e_v + K_{i,v} \int e_v \, dt, & |e_v| > \Delta V \\ 0, & |e_v| \leq \Delta V \end{cases} \quad \dots (45)$$

where, $K_{p,v}$ and $K_{i,v}$ are voltage-loop gains and ΔV defines a dead band to avoid unnecessary reactive power oscillations. For power-factor regulation, the required reactive power ($Q^*$) to achieve the desired power factor, $pf_{ref}$ is computed as

$$Q^* = P \tan(\cos^{-1}(pf_{ref})) \quad \dots (46)$$

and $i_{q,RC} = \frac{2}{3}\frac{(Q^{*}-Q)}{V_d}$. … (47)

This formulation enables dynamic adjustment of reactive current in response to power-factor deviations without necessitating controller re-tuning. The total $q$-axis reference current is given by

$$i_q^{*} = i_{q,ref} + i_{q,RC} \quad \text{… (48)}$$

Block diagram of the proposed FF-FDCC-based grid-connected inverter control implemented in the $d$–$q$ reference frame, is shown in Fig. 4. Compared to conventional d-q control, the FF-FDCC strategy eliminates the need for two sensors by using model-based estimation. Instead of measuring inverter voltages ($V_{td}$, $V_{tq}$) and currents ($i_d$, $i_q$) directly, it estimates them using grid voltage feedback ($V_{gd}$, $V_{gq}$), filter resistance ($R_f$) and inductance ($L_f$). This approach reduces hardware complexity, improves reliability and enhances control speed making it a cost-effective solution for inverter control. A comparison of sensor requirements for conventional d-q control vs. FF-FDCC is presented in Table 1.

**Lyapunov Stability Analysis of FF-FDCC Controller**

The stability of proposed inverter control is evaluated using Lyapunov stability analysis to ensure

Table 1 — Sensor requirements comparison for conventional control vs. FF-FDCC control

| Sensors required | d-q Control | FF-FDCC control | Reason |
|---|---|---|---|
| DC-link voltage | Required | Required | Needed for power control |
| Grid voltage | Required | Required | Required for phase locked loop (PLL) |
| Grid current | Required | Not required | Estimated using the controller model |
| Inverter voltage | Required | Not required | Eliminated using estimated reference voltages |

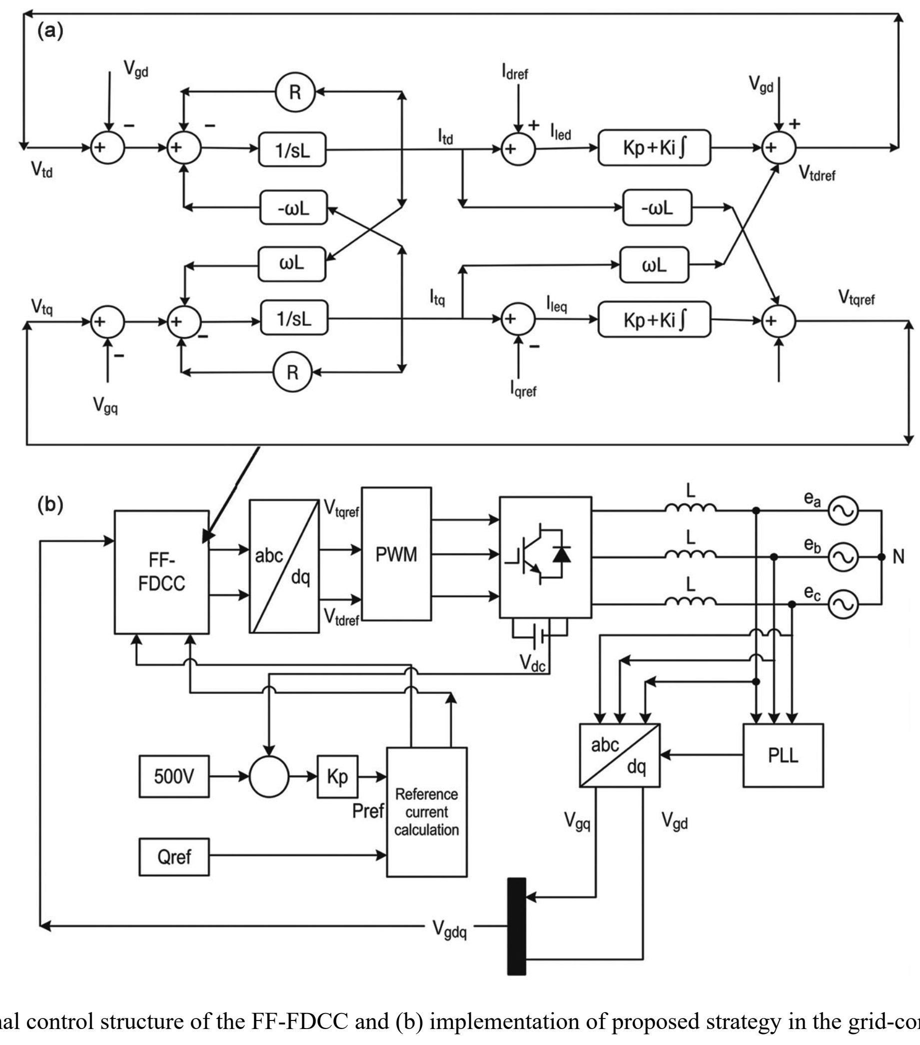


Fig. 4 — (a) Internal control structure of the FF-FDCC and (b) implementation of proposed strategy in the grid-connected inverter

the convergence to a stable equilibrium point. From Eqs (35, 36)

$$\dot{x_1} = \frac{1}{L_f}(-R_f x_1 + V_{tdref} - V_{gd}) \quad \dots (49)$$

$$\dot{x_2} = \frac{1}{L_f}(-R_f x_2 + V_{tqref} - V_{gq}) \quad \dots (50)$$

where, $x_1 = I_d$ and $x_2 = I_q$ are the state variables.

Lyapunov function is chosen as

$$V(x) = \frac{1}{2}L_f({x_1}^2 + {x_2}^2) \quad \dots (51)$$

For asymptotic stability $\dot{V(x)} < 0$; for all $x \neq 0$: The control inputs are designed as

$$V_{tdref} = V_{gd}(s) - K_d x_1 \quad \dots (52)$$

$$V_{tqref} = V_{gq}(s) - K_q x_1 \quad \dots (53)$$

where, $K_d$, $K_q > 0$ are controller gains. Substituting yields

$$\dot{V(x)} = -R_f({x_1}^2 + {x_2}^2) - K_d {x_1}^2 - K_q {x_2}^2 \quad \dots (54)$$

Since $\dot{V(x)}$ is negative definite, the closed-loop system is asymptotically stable.

## Results and Discussion

The proposed DISMC controlled KY converter is first validated using a 400 W PV system to assess MPPT performance under uniform and varying irradiance, focusing on chattering reduction, steady state error, and dynamic tracking. The integrated DISMC–KY and FF–FDCC framework is then extended to a 25 kW PV system for P2V and P2G operation. P2V performance is evaluated through charging efficiency and SOC rise rate, while P2G operation examines power export capability, cross coupling mitigation, dynamic Q compensation and grid power quality compliance. The key PV panel specifications, converter and DISMC parameters used for simulations are listed in Table 2.

### Validation of DISMC-KY Performance

#### *Under Standard Test Conditions (STC)*

Under uniform irradiance (1000 W/m² at 25°C), system performance is evaluated using conventional PI-based control (without DISMC) and the proposed DISMC control. The PI controller serves as a benchmark due to its widespread MPPT use. Both controllers are implemented under identical conditions for fair comparison. The KY converter switching frequency is set to 10 kHz, and performance is assessed using chattering magnitude and steady-state error of $V_{pv}$, as summarized in Table 3.

Chattering magnitude (h) can be computed as follows

$$h = h_1 - h_2. \quad \dots (55)$$

Table 2 — System and controller parameters used for 400 W validation and 25 kW scaling analysis

| Component | Parameter | 400 W (Simulation) | 25 kW (Scaled system) |
|---|---|---|---|
| PV array | Rated PV power (Ppv) | 400W | 25 000W |
| | Voltage at MPP(Vmpp) | 168V | 320V |
| | Current at MPP(Impp) | 2.38A | 83A |
| | Open circuit voltage Voc | 180V | 370V |
| KY converter | Input inductance L | 0.43mH | 8.1mH |
| | Output capacitance Co | 2810μF | 171μF |
| | Converter switching frequency $f_{SW}$ in kHz | 10 | 10 |
| DISMC control | Sliding coefficients $a_1$, $a_2$, $a_3$, $a_4$ | Tuned | Tuned |
| | Integral gains | α=0.6, β=0,9 | α=0.6,β=1.02 |
| Inverter control | Filter inductance | 2.0–3.0 mH | 1.5–2.5 mH |
| | Current controller gains | Kp: 0.5–1.0, Ki: 50–100 | Kp: 2–4, Ki: 200–400 |
| | Inverter switching frequency $f_{SW}$ in kHz | 20 | 20 |

Table 3 — Simulated result under uniform irradiance

| Parameters | Maximum PV power (W) | Average PV power (W) | Tracking time (sec) | Maximum load voltage (V) | Average load voltage (V) | Tracking time (sec) | Average load power (W) | Power conversion efficiency (%) | Steady state error (V) |
|---|---|---|---|---|---|---|---|---|---|
| Without DISMC | 400.4 | 374.1 | 0.872 | 223 | 212.8 | 1.44 | 319.5 | 85.4 | 0.7 |
| With DISMC | 400.4 | 383 | 0.44 | 234 | 220 | 1.1 | 351 | 91.6 | 0.01 |

where, $h_1$ and $h_2$ represent the $V_{pv}$ signal's greatest and lowest chattering points respectively in PV power. Similarly, SSE can be calculated as follows:

$$SSE = Vref - [h_2 + \frac{(h_1 - h_2)}{2}] \quad \dots (56)$$

The efficiency of proposed control is measured using Power Conversion Efficiency (η)

$$\eta = \frac{\text{Average output power across load}}{\text{Average PV power (Converter input power)}} \quad \dots (57)$$

Although the maximum PV power remains constant at 400.4 W, the proposed DISMC enhances the energy utilization by suppressing chattering, thereby increasing the average extracted PV power from 374.1 W to 383 W. DISMC also increases the average load voltage and power with reduced oscillations, resulting in power conversion efficiency improvement from 85.4% to 91.6%.

***Under Partial Shading Conditions***

Partial shading is simulated using three irradiance patterns over a 5-sec time interval with an average irradiance of 925 W/m² (0–2 sec), 775 W/m² (2–3.5 sec), and 625 W/m² (3.5–5 sec). As shown in Table 4, DISMC reduces SSE from 0.7 V to 0.02 V, increases average PV power from 292 W to 302 W, and reduces tracking time from 0.885 sec to 0.638 sec. The average load voltage improves from 197 V to 206 V, while efficiency increases from 80.8% to 90.06%. Supporting waveforms are presented in Fig. 5(a) and (b)

The steady state behaviour of the sliding surface $S$, illustrated in Fig. 5(c) demonstrating that the DISMC drives the PV voltage $V_{pv}$ to the reference voltage $V_{ref}$. Any deviation between $V_{pv}$ and $V_{ref}$ results in a nonzero sliding surface, which is corrected by the DISMC through appropriate adjustment of system dynamics. The bounded fluctuations around zero indicate stable operation, with $S(x)$ remaining below 2 V and consistently converging to zero, thereby satisfying the convergence condition

**Simulation Analysis in P2V Mode**

Following the 400 W simulation validation, the system is scaled to a 25-kW PV system to evaluate the performance in P2V mode. The proposed DISMC increases the average solar power from 23.53 kW to 24.64 kW and battery power from 22.13 kW to 24.16 kW. The settling time of the charging process reduced from 1.5 seconds to 0.36 seconds while the SOC rate improves from 0.000379% to 0.000412% per seconds as shown in Fig. 6(a). The average charging current

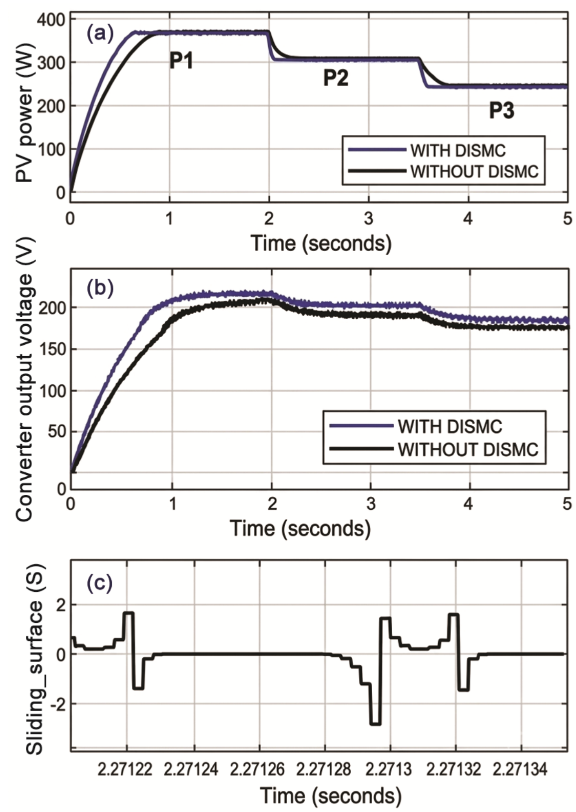


Fig. 5 —Variation in: (a) PV Power (b) Converter output voltage and c) Sliding surface (S) showing error convergence to zero

Table 4 — Simulated result under PSC with and without DISMC

| Control strategy | Maximum PV power (W) | Tracking time (sec) | Average PV power (W) | Maximum load voltage (V) | Average load voltage (V) | Tracking time (sec) | Average load power (W) | Power conversion efficiency (%) | Steady state error |
|---|---|---|---|---|---|---|---|---|---|
| Without DISMC | 367 at P1<br>306.3 at P2<br>253.4 at P3 | 0.885<br>2.34<br>3.65 | 292 | 209 | 197 | 1.9 | 236 | 80.8 | 0.7 |
| With DISMC | 367 at P1<br>306.4 at P2<br>253.4 at P3 | 0.638<br>2.1<br>3.05 | 302 | 217 | 206 | 1.15 | 272 | 90.06 | 0.02 |

rises from 71.2 A to 75.4 A, thereby reducing the charging time ($T_{ch}$), which is determined by

$$T_{ch} = C_{bat} \frac{(SOC_{final} - SOC_{initial})}{I_{avg}} \quad \dots (58)$$

where, $C_{bat}$ is battery capacity and $I_{avg}$ is average charging current. This results in 4% improvement in solar power tracking and 9% increase in battery charging power. Simulated results in Table 5 validate the findings. The DC-link voltage is stabilized at 500 V before feeding the charger circuit as shown in Fig. 6(b).

**Simulation Analysis in P2G Mode**

The performance of the proposed FF-FDCC strategy in P2G operation is evaluated under irradiance level of 1000W/m², 900W/m², and 750W/m². Inverter operates at switching frequency of 20 kHz to reduce output current ripple, improve THD performance and mitigate EMI. The grid filter parameters ($L_f$, $R_f$) are designed to satisfy harmonic attenuation requirements and comply with IEEE-519 and IEC-61000-3-2 standards.

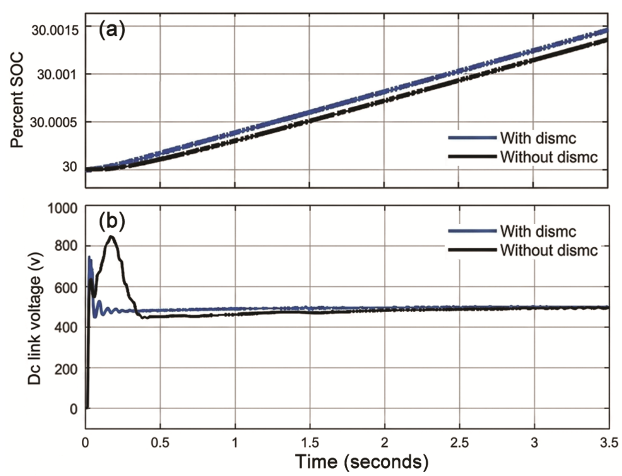


Fig. 6 — (a) % SOC comparison and (b) Stabilization of DC link voltage to 500V with and without DISMC

As shown in Table 6, the average solar power delivered to the grid remains nearly identical for both conventional d–q control (23.53 kW) and FF-FDCC (23.64 kW). However, FF-FDCC eliminates reactive power oscillations and maintains nearly zero reactive power (Q≈0) under PSC without controller re-tuning as shown in Fig. 7. The resulting grid current becomes nearly sinusoidal, reducing THD from 31.99% to 3.27%, demonstrating significant improvement in power quality.

**Dynamic Reactive Power Compensation using FF-FDCC**

To evaluate the capability of the proposed FF-FDCC strategy for reactive power compensation without controller re-tuning in P2G mode, step changes are applied to the reactive current reference $i_q^{ref}$ to emulate unity, leading, and lagging power factor operation. As shown in Fig. 8(a), the $d$-axis current remains regulated around 50 A, while the $q$-axis current accurately follows step variations of ±10 A. The current tracking error in Fig. 8(b) rapidly converges to zero, confirming stable reactive power regulation without controller re-tuning.

**State-Space Switching in P2V and P2G Modes**

The proposed power management module employs a state-space switching strategy to enable seamless transitions between P2V and P2G modes by monitoring battery SOC and available PV power as shown in Fig. 9. In P2V mode, charging occurs when EV battery SOC is below its maximum limit and the DC-link voltage exceeds the EV battery voltage. In P2G mode, surplus PV power is exported to the grid once battery is fully charged. The primary state variables are battery SOC and grid power ($P_{grid}$), with PV power ($P_{PV}$) as input. The binary control inputs $u_1$ (P2V) and $u_2$ (P2G) regulates the power flow. State-space model is expressed as:

$$\frac{d}{dt}\begin{bmatrix} SOC_{EV} \\ P_{grid} \end{bmatrix} = \begin{bmatrix} \frac{P_{PV}}{C_{EV}V_{EV}} u1 \\ \frac{P_{grid}}{C_{grid}V_{grid}} u2 \end{bmatrix} \quad \dots (59)$$

Table 5 — Simulated result of solar EV charging with and without DISMC

| Parameters | Average solar power (kW) | Average battery power (kW) | Settling time (sec) | SOC charging rate (% /sec) | Average charging current (A) | Maximum charging current (A) | Power conversion efficiency (%) |
|---|---|---|---|---|---|---|---|
| Without DISMC | 23.53 | 22.13 | 1.5 | 0.000379 | 71.2 | 76 | 94.05 |
| With DISMC | 24.64 | 24.16 | 0.36 | 0.000412 | 75.4 | 78 | 98.05 |

Table 6 — Simulated Result of P2G mode with dq control and FF-FDCC

| Battery parameters | Average solar power (kW) | Grid power (kW) | THD | Active power P (kW) | Reactive power Q (kVAr) |
|---|---|---|---|---|---|
| d-q control | 23.53 | 19.13 | 31.9 | 19.13 | 1 |
| FF-FDCC | 23.64 | 22.46 | 3.27 | 22.46 | 0 |

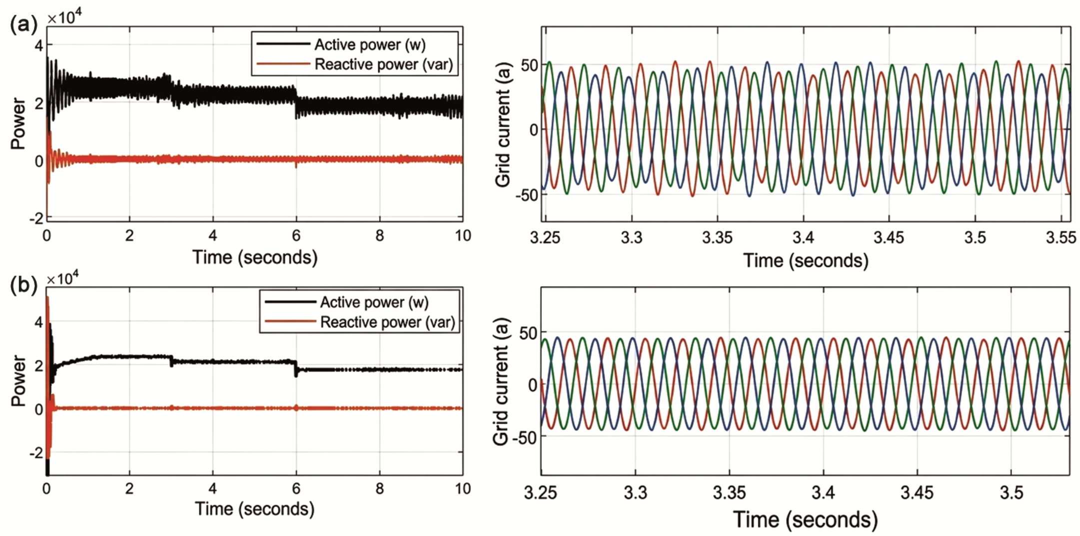


Fig. 7 — Variation of active and reactive power and the corresponding grid current under: (a) conventional dq control, (b) FF-FDCC

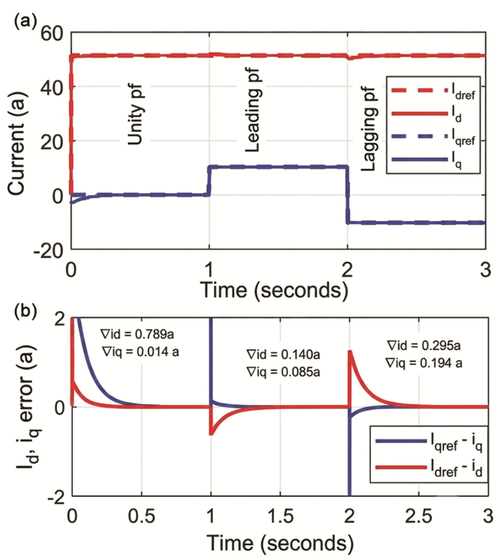


Fig. 8 — (a) Grid current references and responses under unity, leading, and lagging power factor operation, (b) $d$ *and* $q$ axis current tracking error during reactive power transitions

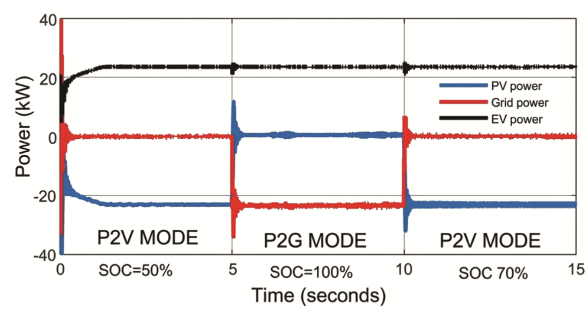


Fig. 9 — Seamless transition in P2V and P2G mode

For P2V Mode,

$$u1 = \begin{cases} 1, \text{if } P_{PV} > P_{EV} \text{ and } SOC_{EV} < SOC_{EV}^{MAX} \\ 0, \text{Other wise} \end{cases} \quad \ldots (60)$$

For P2G Mode ,

$$u2 = \begin{cases} 1, \text{if } P_{PV} > 0 \textit{ and } SOC_{EV} > SOC_{EV}^{MAX} \\ 0, \text{Other wise} \end{cases} \quad \ldots (61)$$

**Harmonic Spectral Analysis and EMI Assessment**

The effectiveness of the proposed controller in mitigating EMI is evaluated using frequency-domain analysis. FFT analysis of the converter output voltage and inverter current is performed to examine switching harmonics at the fundamental switching frequency and its multiples. The FFT spectrum up to 40 kHz in Fig. 10(a) shows harmonic attenuation of 14.1 dB at $f_{sw}$, 33.5 dB at $2f_{sw}$, and 24.4 dB at $3f_{sw}$ compared to conventional control, confirming suppression of switching harmonics. The peak-to-peak ripple in KY converter voltage decreases from 7.5 V to 2.1 V with DISMC, resulting in a reduced voltage slew rate (dV/dt) and lower EMI generation.

The grid current FFT spectrum within 20 kHz ± 20 kHz is shown in Fig. 10(b), where the inverter switching frequency ($f_{sw}$ = 20 kHz) and its second harmonic are observed. The proposed FF-FDCC strategy achieves attenuation of 20 dB at $f_{sw}$ and 22.9 dB at $2f_{sw}$, indicating reduced high-frequency EMI propagation. Also, dominant harmonics are effectively suppressed, ensuring compliance with IEC 61000-3-2 and IEEE 519 standards.[37,38] Conducted EMI evaluation using a CISPR 11 LISN setup shows a 10–13 dB compliance margin improvement.[39,40] A comparison of harmonic distortion and conducted EMI performance for the conventional dq control and the proposed FF-FDCC is shown in Figs. 11(a) and (b) respectively.

### Benchmarking Against State-of-the-Art Control Strategies

To benchmark the proposed DISMC-KY and FF-FDCC based PV–EV–grid integrated system, a comparative evaluation has been conducted against converter control strategies and recent state-of-the-art grid connected PV systems as summarized in Tables 7 and 8.

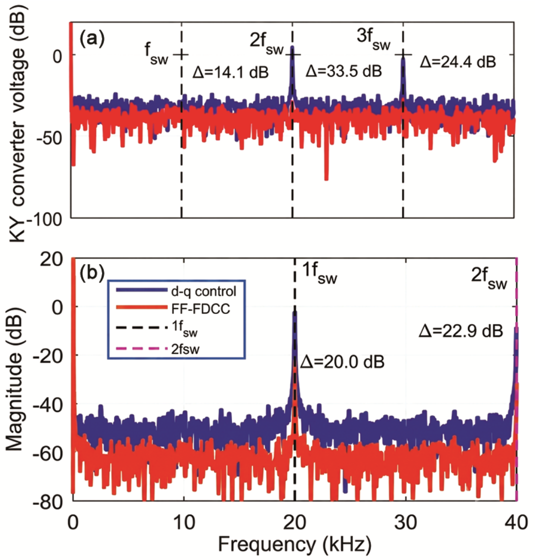


Fig. 10 — FFT spectrum of (a) KY converter output voltage (b) Grid current

## Proposed Control System Validation

### DC-Side Hardware Validation

In the experimental setup, a 40W PV panels is used to evaluate the effectiveness of the proposed DISMC under realistic conditions.

Initially, the KY converter is tested in the laboratory using a 20 V DC input with a duty cycle of

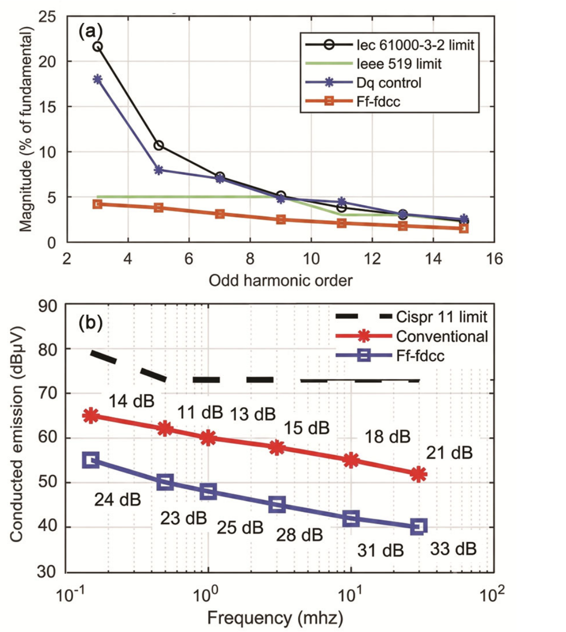


Fig. 11 — Harmonic and EMI performance comparison for conventional dq control and FF-FDCC: (a) Harmonic spectrum with IEC 61000-3-2 and IEEE 519 limits, (b) CISPR 11 conducted EMI emission comparison.

Table 7 — Comparison of the Proposed DISMC – KY MPPT with Advanced MPPT approaches

| Literature reference No | Proposed system | Monish *et al.*[26] | Rahul & Hariharan[19] | Ghazi *et al.*[23] | Waghmare & Chaturvedi[24] |
|---|---|---|---|---|---|
| Converter topology | KY converter | DC–DC converter | Boost converter | Boost converter | Flyback converter |
| MPPT control | InC based DISMC | Qlearning + ANN + regression based MPPT | DISMC | CSA tuned SuperTwisting SMC | HigherOrder SMC with supertwisting |
| MPPT tracking time | 0.44 sec under STC 0.638 sec under PSC | Value not stated | ≈0.035 s | Value not stated | Value not stated |
| Chattering | Effectively eliminated | Data driven control | Reduced | Effectively eliminated | Effectively eliminated |
| MPPT efficiency | 98.05 % (25 kW) | Improved but value not quantified | ≈99 % | Improved but value not quantified | Not quantified |
| Rated power level | 40 W (hardware) , 400W/25kW (simulation) | Low power range (≈1–10 W) | 1 kW PV system (simulation) | 100 kW PV system (simulation) | 12 W PV system (simulation) |
| Grid integration | Yes | No | No | Yes | No |
| Control complexity | Moderate and hardware feasible | High; data driven, training dependent | Moderate; nonlinear SMC | High; metaheuristic tuned SMC | High; higher order nonlinear control |

Table 8 — Benchmarking of the proposed framework against recent grid-connected PV control approaches

| Literature reference No | Hakam *et al.*[42] | Jain & Singh[41] | Watil & Chojaa[43] | Astaomar & Erkal[4] | Proposed System |
|---|---|---|---|---|---|
| Control method | ANN–Kalman filter + MPC | Positive sequence component + PI + Hysteresis | MPC | InC-SMC | DISMC-KY + FF-FDCC |
| Decoupling | Predictive | Positive sequence | Adaptive power | dq decoupling | Feedforward |
| Stability analysis | MPC stability | PI tuning | PIL validation | Lyapunov | Lyapunov + Bode |
| Sensors used | ~6 sensors | ~7 sensors | ~5 sensors | ~5 sensors | ~3 sensors |
| MPPT strategy | ANN-KF | Conventional | Not applicable | InC-SMC | InC + DISMC |
| Grid THD | 0.56% | 2.98–3.32% | Not reported | ~3% | 3.27% |
| Power factor | Near unity | 0.998 | Adjustable | Unity | Unity PF |
| Reactive power control | Not addressed | Via $Q_{ref}$ | Independent Q control | dq control | Dynamic compensation |
| Grid support | V2G | V2G + peak shaving | Voltage/frequency support | Grid injection | P2G + reactive support |

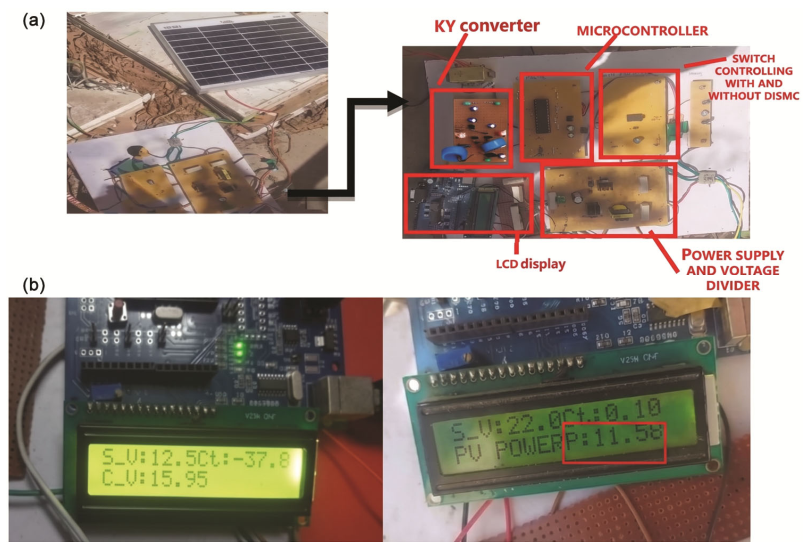


Fig. 12 — (a) Experimental Lab setup, (b) Converter output voltage and PV power with DISMC

0.7. Without DISMC, the converter produces 30 V, whereas with DISMC the output increases to 34 V, indicating improved voltage regulation. Further validation under PSC is performed in an outdoor setup as shown in Fig. 12(a) is implemented. Without DISMC, the converter output reaches 13.36 V for a 12.5 V panel voltage, while with DISMC it increases to 15.95 V. Experimental results in Fig. 12(b) show PV power increasing from 10.15 W to 11.58 W. The prototype achieves a peak PV power of 36.5 W, producing converter output of 44 V with average load performance of 39 V and 33.5 W with a 50 Ω load.

**Per-Unit Scaling and Power Level Validation**

Scaling and extrapolation of the proposed DISMC–KY converter are performed using per-unit normalization to relate the 40 W prototype to 400 W and 25 kW systems, as summarized in Table 9. Voltage and power scaling ratios are approximately 1:10 and 1:625. Experimental results show deviations within 10% for PV voltage and 15% for converter output voltage. The prototype delivers an average output power of 36.5 W, closely matching scaled simulation predictions.

**Grid-Side Stability Assessment**

The grid-side stability of the proposed FF-FDCC strategy is verified through lyapunov analysis and bode plot evaluation. From Eqs (49–54), the lyapunov function $V(x)$ is positive definite and its derivative $\dot{V}(x)$ is negative definite, ensuring asymptotic stability. as shown in Fig. 13(a), $V(x)$ decreases monotonically while $\dot{V}(x)$ remains negative, confirming stable convergence. this results in reduced oscillations, improved dynamic response, and enhanced tracking accuracy for reliable inverter control.

Table 9 — Scaling and deviation analysis of the prototype and simulated PV systems

| Measured Parameter | 40 W prototype (Measured value) | Scaled from 400 W (Measured value in 400 W /Scale ratio) | Deviation (± %) | Scaled from 25 kW (Measured value in 25 kW /625) | Deviation (± %) |
|---|---|---|---|---|---|
| PV power (Pmax) at STC | 36.5 W | 383 / 10 = 38.3 W | − 4.9 % | 24 640 / 625 = 39.4W | − 7.4% |
| PV voltage at Pmax | 30.5 V | 156 / 5.25 = 29.7 V | 2.60% | 316 / 10 = 31.6 V | − 3.5 % |
| KY converter output voltage | 44 V | 252 / 5.25 = 48 V | − 8.3 % | 512 / 10 = 51.2 V | − 14.1 % |
| Converter output current | 36.5 ÷ 44 = 0.83 A | 383 / (252x1.9) = 0.8 A | 3.8% | 24640/(512 x62.4) = 0.78 A | 6.40% |
| Average load voltage | 39 V | 220 / 5.25 = 41.9 V | − 7.0 % | 440 / 10 = 44 V | − 11.3 % |
| Average load power | 33.5 W | 351 / 10 = 35.1 W | − 4.6 % | 21 900 / 625 = 35.0 W | − 4.5 % |

To evaluate the robustness of the proposed FF-FDCC strategy against grid impedance variations, a detailed Bode plot–based analysis is performed using the derived inverter current-loop model. The open-loop Bode magnitude plots of FF-FDCC for different grid resistance values (0.6 $R_g$ to 1.4 $R_g$) are as in Fig. 13(b).

The plant transfer function is

$$G_p(s) = \frac{1}{L_{eq}s+R_{eq}} \quad \dots (62)$$

where, $L_{eq} = L_f + L_g$ and $R_{eq} = R_f + R_g$, and the proportional–integral (PI) controller is

$$G_c(s) = K_p + \frac{K_i}{s} \quad \dots (63)$$

where, $K_p$ is the proportional gain, $K_i$ is the integral gain,

Thus, the open-loop transfer function used for Bode analysis is

$$G_{OL}(s) = \frac{K_p s+K_i}{s(L_{eq}s+R_{eq})} \quad \dots (64)$$

while the closed-loop current transfer function (CLTF) for pole-zero plot is

$$G_{CL}(s) = \frac{K_p s+K_i}{L_{eq}s^2+(R_{eq}+K_p)s+K_i} \quad \dots (65)$$

The gain crossover occurs at a frequency well above the fundamental grid frequency (50 Hz) and significantly below the inverter switching frequency ($f_{sw}$ = 20 kHz), ensuring a clear separation between the control bandwidth and high-frequency switching dynamics. This separation confirms that the FF-FDCC-based current loop remains stable with adequate phase and gain margins, thereby satisfying the frequency-stability equilibrium condition. Minor oscillatory peaks observed near the switching frequency arise from the interaction between inverter switching harmonics and the $L_g$–$C_f$ filter resonance. These peaks remain well below the 0 dB line, ensuring that switching-frequency oscillations do not influence the closed-loop response. The combined damping effect of the filter and grid resistances $(R_f + R_g)$, together with the feed-forward decoupling structure, effectively suppresses resonance amplification. As a result, the proposed FF-FDCC controller maintains stable and well-damped operation without requiring controller retuning under grid impedance variations. This behaviour is further

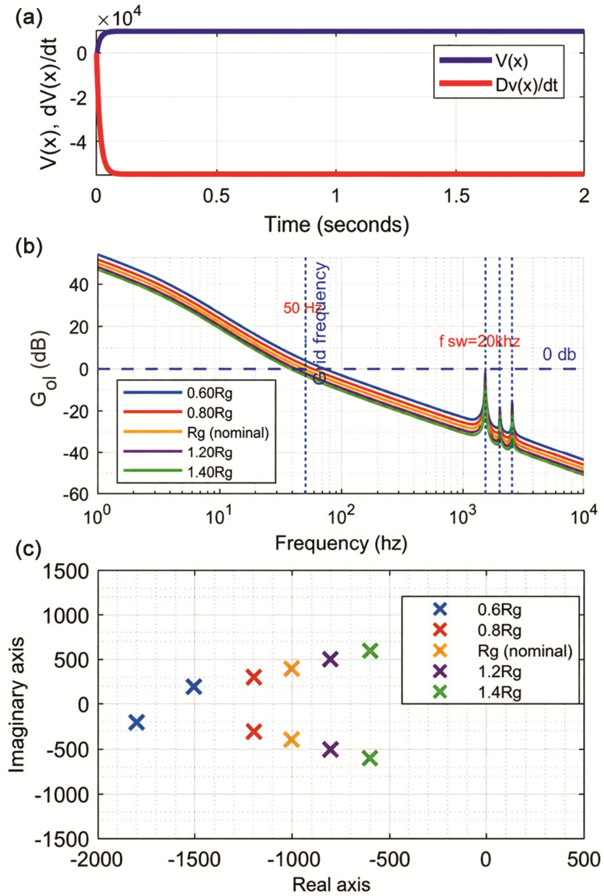


Fig. 13 — (a) Stability analysis using lyapunov method (b) Open-loop bode magnitude of FF-FDCC for different grid resistance values ($0.6R_g$–$1.4R\_g$) and (c) Closed-loop pole locations under grid resistance variations

confirmed in Fig. 13(c), where all closed-loop poles corresponding to varying grid resistance conditions remain well within the left-half plane with sufficient separation from the imaginary axis, ensuring stable and well-damped system operation.

## Conclusions

This paper presented an integrated control framework for grid connected solar EV charging based on a DISMC controlled KY converter for DC-side MPPT and a FF-FDCC strategy for AC-side inverter regulation. The proposed approach presents the first DISMC formulation applied to a KY converter in a PV–EV system, enabling fast and accurate global MPP tracking with improved power conversion efficiency, negligible chattering and steady-state error, which in turn leads to reduced EV charging time. On the grid side, the FF-FDCC strategy eliminated d–q axis cross coupling, reduced current distortion and improved active power injection with minimal sensor dependency. Experimental validation using a 40 W DC-side hardware prototype, simulation-based verification on a 400 W system, and system-level evaluation on a 25-kW PV–EV charging model with seamless surplus power export have been carried out in this work. Future work will focus on grid fault ride-through capability, DVR-assisted power quality enhancement, bidirectional V2G operation, and full-scale AC-side hardware implementation to validate fault resilience and uninterrupted EV charging under practical grid disturbances.

## References


1 Kumar M, Panda K P, Rosas-Caro J C, Valderrabano-Gonzalez A & Panda G, Comprehensive review of conventional and emerging maximum power point tracking algorithms for uniformly and partially shaded solar photovoltaic systems, *IEEE Access*, (**11**), (2023), 31778–31812, doi:10.1109/ACCESS.2023.3262502.

2 Harrison A, Alombah N H & de Dieu Nguimfack Ndongmo J, A new hybrid MPPT based on incremental conductance-integral backstepping controller applied to a PV system under fast-changing operating conditions, *Int J Photoenergy, (*2023), 1–17, doi:10.1155/2023/9931481.

3 Messaoudi F, Farhani F & Zaafouri A, A new approach to MPPT hybrid incremental conductance-sliding mode control for PV grid-connected systems, *Meas Control*, **57(9**) (2024) 1370–1382, doi:10.1177/00202940241240666.

4 S Astaomar & B Erkal, "Improving the performance of an incremental conductance MPPT algorithm using harris-hawks optimization in photovoltaic systems," *IEEE-GEC*, (2024), 128–134, doi:10.1109/GEC61857.2024.10881949.

5 Bouarroudj N, Benlahbib B, Houam Y, Sedraoui M, Batlle V F, Abdelkrim T, Boukhetala D & Boudjema F, Fuzzy based incremental conductance algorithm stabilized by an optimal integrator for a photovoltaic system under varying operating conditions, *Energy Sources Part A-Recovery Util Environ Eff*, **47(1)** (2025) 9682–9707, doi:10.1080/15567036.2021.1955049.

6 Mishra D P, Senapati R & Salkuti S R, Comparison of DC-DC converters for solar power conversion system, *Indones J Electr Eng Comput Sci*, **26(2)** (2022) 648–655, doi:10.11591/ijeecs.v26.i2.

7 Amri B & Ashari M, The comparative study of Buck-boost, Cuk, Sepic and Zeta converters for maximum power point tracking photovoltaic using P&O method, *2nd Int Conf Informat Technol Comput Electr Eng*, (2015) 327–332, doi:10.1109/ICITACEE.2015.7437823.

8 Mumtaz F, Zaihar Yahaya N, Tanzim Meraj S, Singh B, Kannan R & Ibrahim O, Review on non-isolated DC-DC converters and their control techniques for renewable energy applications, *Ain Shams Eng J*, **12(4)** (2021) 3747–3763, doi:10.1016/j.asej.2021.03.022.

9 Jin F, Nabih A, Chen C, Chen X, Li Q & Lee F C, A high efficiency high density DC/DC converter for battery charger applications, IEEE *APEC*, (2021) 1767–1774, doi:10.1109/APEC42165.2021.9487108.

10 Silva A W, Bezerra L D, Jucá S C, Pereira R I & de Sá Medeiros C M, Control and monitoring of a Flyback DC-DC converter for photovoltaic applications using embedded IoT system, *IEEE Lat Am Trans*, **18(11)** (2021) 1892–1899, doi:10.1109/TLA.2020.9398630.

11 Leal W C, Godinho M O, Bastos R F, de Aguiar C R, Fuzato G H & Machado R Q, Cascaded interleaved DC–DC converter for a bidirectional electric vehicle charging station, *IEEE Trans Ind Electron*, **71(4)** *(*2023) 3708–3717, doi:10.1109/TIE.2023.3273281.

12 Sutikno T, Samosir A S, Aprilianto R A, Purnama H S, Arsadiando W & Padmanaban S, Advanced DC–DC converter topologies for solar energy harvesting applications: A review, *Clean Energy*, **7(3)** (2023) 555–570, doi:10.1093/ce/zkad003.

13 Kumar K R, Raja K R, Padmanaban S, Muyeen S M & Khan B, Comprehensive review of KY converter topologies, modulation and control approaches with their applications, *IEEE Access*, (**10**) (2022) 20978–20994, doi:10.1109/ACCESS.2022.3151697.

14 Vasumathi G, Jayalakshmi V & Sakthivel K, Efficiency analysis of grid tied PV system with KY integrated SEPIC converter, *Meas Sens*, (**27**) (2023) 100767, doi:10.1016/j.measen.2023.100767.

15 Wu L, Liu J, Vazquez S & Mazumder S K, Sliding mode control in power converters and drives: A review, *IEEE/CAA J Autom Sin*, **9(3**) (2022) 392–406, doi:10.1109/jas.2021.1004380.

16 Dunna V K, Chandra K P, Rout P K & Sahu B K, Design and real-time validation of higher order sliding mode observer-based integral sliding mode MPPT control for a DC microgrid, *IEEE CJECE*, **45(4)** (2022) 418–425, doi:10.1109/ICJECE.2022.3211470.

17 Yılmaz M, Kaleli A & Çorapsız M F, Machine learning based dynamic super twisting sliding mode controller for increase speed and accuracy of MPPT using real-time data

under PSCs, *Renew Energy*, **(219)** (2023) 119470, doi:10.1016/j.renene.2023.119470.

18 Kayisli K, Super twisting sliding mode-type 2 fuzzy MPPT control of solar PV system with parameter optimization under variable irradiance conditions, *Ain Shams Eng J*, **14(1)** (2023) 101950, doi:10.1016/j.asej.2022.101950.

19 I Rahul & R Hariharan, Enhancement of solar PV panel efficiency using double integral sliding mode MPPT control, *Tsinghua Sci Technol*, **29 (1)** (2024) 271–283, doi:10.26599/TST.2023.9010030.

20 C S Anjumol & P Thekkath, Performance assessment of P&O-based and InC-based double integral sliding mode control MPPT for a solar photovoltaic system and DC voltage enhancement using synchronous boost converter, *IEEE Int Conf Futurist Tech Control Syst & Renew Energy*, (2024) 1–6, doi:10.1109/ICFCR64128. 2024.10763084.

21 Pradhan R, Design of observer-based robust double integral sliding mode controller for grid-connected PV system, *Power Quality in Microgrids: Issues, Challenges and Mitigation Techniques*, (2023) 429–449.

22 B Torchani, A T Azar, A Sellami, S Ahmed, I A Hameed, I Kasim Ibraheem & Al-Obaidi, Adaptive sliding mode control based on maximum power point tracking for boost converter of PV system under reference voltage optimizer, *Front Energy Res*, **(12)** (2024) 1485470, doi:10.3389/fenrg. 2024.1485470.

23 G A Ghazi, E A Al-Ammar, H M Hasanien, W Ko, S M Lee, R A Turky, M Tostado-Véliz & F Jurado, Circle search algorithm-based super twisting sliding mode control for MPPT of different commercial PV modules, *IEEE Access*, **(12)** (2024) 33109–33128, doi: 10.1109/ACCESS. 2024.3372412.

24 T T Waghmare & P Chaturvedi, Super twisting approach of a higher order sliding mode controller for a flyback DC–DC converter in photovoltaic applications, *Int J Circuit Theory Appl,* **51(9)** (2023) 4202–4219, doi:10.1002/cta.3636.

25 D Mazumdar, C Sain, P K Biswas, P Sanjeevi kumar & B Khan, Overview of solar photovoltaic MPPT methods: A state-of-the-art on conventional and artificial intelligence control techniques, *Int Trans Electr Energ Syst,* **(1)** (2024) 8363342, doi:10.1155/2024/8363342.

26 B S Monish, N A Sai, S R Karnati, R Kumar & D K Sah, AI-based solar energy harvesting: MPPT using machine learning algorithms, *Int Conf on RAIT*, (2025) 1–5, doi: 10.1109/RAIT65068.2025.11089447.

27 O N Nezamuddin, C L Nicholas & E C dos Santos, The problem of electric vehicle charging: State-of-the-art and an innovative solution, *IEEE Trans Intell Transp Syst,* **23(5)** (2021) 4663–4673, doi:10.1109/tits.2020.3048728.

28 Liu B, Song Z, Yu B, Yang G & Liu J, A feedforward control-based power decoupling strategy for grid-forming grid-connected inverters, *Energies*, **17(2)** (2024) 424, doi:10.3390/en17020424.

29 Z Gong, C Liu, Y Gui, F F da Silva & C L Bak, Power decoupling method for voltage source inverters using grid voltage modulated direct power control in unbalanced system, *IEEE Trans Power Electron*, **38(3)** (2023) 3084–3099, doi: 10.1109/TPEL.2022.3220436.

30 Singh J K & Behera R K, 2021 An improved hysteresis current controller for grid-connected inverter system to address power quality issues at reduced switching frequency, *IEEE Trans Ind Appl*, **57(2)** (2021) 1892–1901, doi:10.1109/TIA.2021.3052426.

31 N Upadhyay, N P Padhy & P Agarwal, Grid-current control with inverter-current feedback active damping for LCL grid-connected inverter, *IEEE Trans Ind Appl*, **60(1)** (2024) 1738–1749, doi:10.1109/TIA.2023.3316997.

32 Kumar S, Khan K R, Srinivas V L, Shankar G, Saket R K & Jana K C, Electric vehicle fast charging integrated with hybrid renewable sources for V2G and G2V operation, *IEEE Trans Ind Appl*, (2025) 1–14, doi:10.1109/tia.2025.3585855.

33 Kuruvilla V, Kumar P V & Selvakumar A I, Challenges and Impacts of V2g Integration-A Review, *8th Int Conf Adv Comput Commun Syst*, *IEEE*, **(1)** (2022) 1938–1942, doi: 10.1109/ICACCS54159.2022.9785095.

34 A K Gupta, R K Pachauri, T Maity, Y K Chauhan, O P Mahela, B Khan & P K Gupta, Effect of various incremental conductance MPPT methods on the charging of battery load feed by solar panel, *IEEE Access*, **(9)** (2021) 90977–90988, doi:10.1109/ACCESS.2021.3091502.

35 B H Zahra, K Saber & H M Ali, Mitigating Chattering Phenomenon for Photovoltaic System Using Sliding Mode Control Under Rapid Irradiation Level Variation, *IEEE 11th Int Conf Systems Control,* (2023), 567–572, doi: 10.1109/ICSC58660.2023.10449729.

36 Kumar N & Sharma A, Design and analysis of nonlinear controller for a standalone photovoltaic system using Lyapunov stability theory, *J Sol Energy Eng*, **144(1)** (2022) 011003, doi:10.1115/1.4051584.

37 Shan P, Sun Y, Sun K, Song Y, Wu X & Li Q, New metric recommended for the harmonic standard of power electronic distribution systems, *IEEE Ind Appl Soc Annu Meet*, (2023) 1–7, doi: 10.1109/IAS54024.2023.10406768.

38 Shelar S, Bankar D & Bakre S, Review of revisions of IEEE 519 Standard on Power System Harmonics (1981 to 2022), *21st Int Conf Harmon Qual Power*, 2024, 415–420, doi: 10.1109/ICHQP61174.2024.10768696.

39 Wu X, Grande A, Liu X, Grassi F, Spadacini G, Pignari S A, Vallarino F & Ghezzi L, A simple cable radiated emission evaluation method for table-top setups according to CISPR 11 and CISPR 32, *IEEE Access,* **(13)** (2025) 19040–19048, doi:10.1109/ACCESS.2025.3532460.

40 Khilnani A, Wan L, Sumner M, Thomas D, Hamid A & Grassi F, Conducted emissions measurements in DC grids: Issues in applying existing LISN topologies and possible solutions, *IEEE 15th Int Conf Compat Power Electron Power Eng*, (2021) 1–6, doi: 10.1109/CPE-POWERENG50821. 2021.9501169.

41 Jain V & Singh B, A grid connected PV array and battery energy storage interfaced EV charging station, *IEEE Trans Transp Electrif*, **9(3)** (2023) 3723–3730, doi:10.1109/ TTE.2023.3234994.

42 Hakam Y, Ahessab H, Gaga A, Tabaa M & Hadadi B El, Design and simulation of a 5 KW solar-powered hybrid electric vehicle charging station with a ANN–Kalman filter MPPT and MPC-based inverter control for reduced THD, *Sci African*, **(27)** (2025) 02563, doi:10.1016/ j.sciaf.2025.e02563.

43 Watil A & Chojaa H, Enhancing grid-connected PV-EV charging station performance through a real-time dynamic power management using model predictive control, *Results Eng*, **(24)** (2024) 103192, doi:10.1016/j.rineng. 2024.103192.